Intrachain Exciton Motion Can Compete with Interchain Hopping in Conjugated Polymer Films with a Strong J-aggregate Property

Yasuhiro Murata [1] and Yasunari Tamai[1,2] *

[1] Department of Polymer Chemistry, Graduate School of Engineering, Kyoto University, Katsura, Nishikyo, Kyoto 615-8510, Japan

[2] Japan Science and Technology Agency (JST), PRESTO, 4-1-8 Honcho Kawaguchi, Saitama 332-0012, Japan

AUTHOR INFORMATION

Corresponding Author

*E-mail: tamai@photo.polym.kyoto-u.ac.jp

ABSTRACT

Understanding exciton diffusion properties in organic semiconductor films is crucial for organic solar cells because excitons need to diffuse to an electron donor/acceptor interface to dissociate into charges. We previously found that singlet excitons generated in the thin films of a novel naphthobisoxadiazole-based low-bandgap polymer PNOz4T exhibit two-dimensional exciton diffusion characteristics along the backbone and π-stacking directions owing to the HJ-aggregate property of PNOz4T. However, the diffusion constants along these directions could not be determined owing to the difficulty of data analysis. Herein, we present a detailed analysis based on a simulated annealing metaheuristic. We found that intrachain exciton motion can be faster than interchain hopping. Based on temperature dependence measurements, we found that exciton diffusion is more favorable at lower temperatures because the coherent component partly contributes to exciton motion.

TOC GRAPHICS
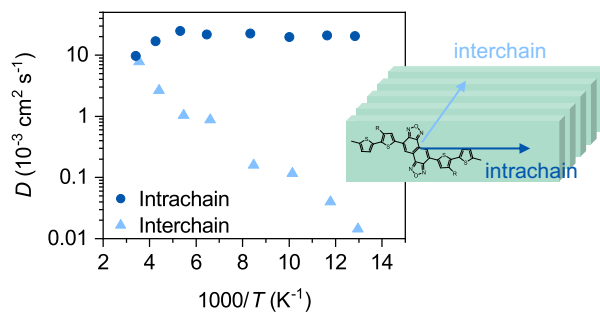
KEYWORDS (Word Style "BG_Keywords"). Exciton diffusion, HJ-aggregate, transient absorption, simulated annealing, Marcov chain Monte Carlo method

The efficient transport of excitons generated in organic semiconducting films is crucial for organic solar cells because excitons need to diffuse to an electron donor/acceptor interface to dissociate into charges. The diffusion of singlet excitons in conjugated polymer films can be considered as a series of Förster energy transfers;[1-4] thereby, interchain exciton hopping is presumed to be faster than intrachain hopping because the Förster mechanism is a long-range resonant energy transfer mediated by dipole–dipole interaction.[5-8] This results in anisotropy of exciton diffusion in the crystalline domains of conjugated polymer films. For instance, we reported that singlet excitons generated in poly(3-hexylthiophene) (P3HT) crystalline domains predominantly diffuse along the π-stacking direction owing to greater interchain exciton coupling.[9-11]

A novel low-bandgap polymer PNOz4T (the chemical structure is shown in Figure 1a) exhibits a strong tendency to form crystalline domains in thin films with a π-π stacking distance of 3.5 Å and lamellar distance of 22 Å.[12,13] Recently, we found that PNOz4T is likely to form HJ-aggregates owing to the relatively high backbone planarity.[14] We studied the exciton diffusion dynamics in pristine PNOz4T films using transient absorption (TA) spectroscopy. By analyzing the excitation fluence dependence of singlet exciton decay including singlet–singlet exciton annihilation (SSA), we revealed that singlet excitons generated in PNOz4T crystalline domains diffuse two-dimensionally (2D) along the backbone and π-stacking directions. However, details of the diffusion properties, such as diffusion constants along both directions, have not been fully elucidated owing to the difficulty of data analysis. This is partly because there exists no simple analytical formula for the rate equation of exciton decay including SSA with anisotropic 2D diffusion because of symmetry reduction (see the Supporting Information for more details).

As an alternative approach, direct observation of exciton motion in well-ordered P3HT nanofibers using transient absorption microscopy (TAM) has been reported, wherein the authors found that a high diffusion constant of up to 1.1 ± 0.1 cm^2 s^{-1} can be achieved in organic semiconductors.[15] The advantage of direct observation using TAM over conventional spatially averaged TA spectroscopy measurements is that it does not require any analytical models. In contrast, the application of TAM is limited to highly diffusive materials due to the limitation of spatial resolution. Therefore, quantifying the diffusion properties of materials with moderate diffusion constant still relies on analysis-based TA spectroscopy measurements, and hence improvement in TA data analysis is pivotal to gain more insights into the exciton diffusion dynamics in organic semiconductors.

Herein, we applied a simulated annealing (SA) metaheuristic,[16] which is a versatile and robust optimization method that can be applied to any complex optimization problem to overcome the so-called "local minima issue". The SA metaheuristic enables us to reach a global minimum solution no matter how complex the objective function is, and no matter how difficult it is to provide a plausible initial condition for the optimization, which allows accurate analysis with minimal approximations that often oversimplify the phenomenon. We demonstrated a detailed analysis of the aforementioned complex anisotropic 2D exciton diffusion behavior of singlet excitons in PNOz4T thin films using a SA metaheuristic. We found that intrachain exciton motion can be faster than interchain hopping. Temperature dependence measurements revealed that exciton motion is more favorable at lower temperatures as opposed to the conventional Arrhenius-type thermally activated diffusion observed in various conjugated polymer films. This thermally de-activated exciton diffusion behavior can be rationalized by taking into account the partial contribution of the coherent transport.[17-21]
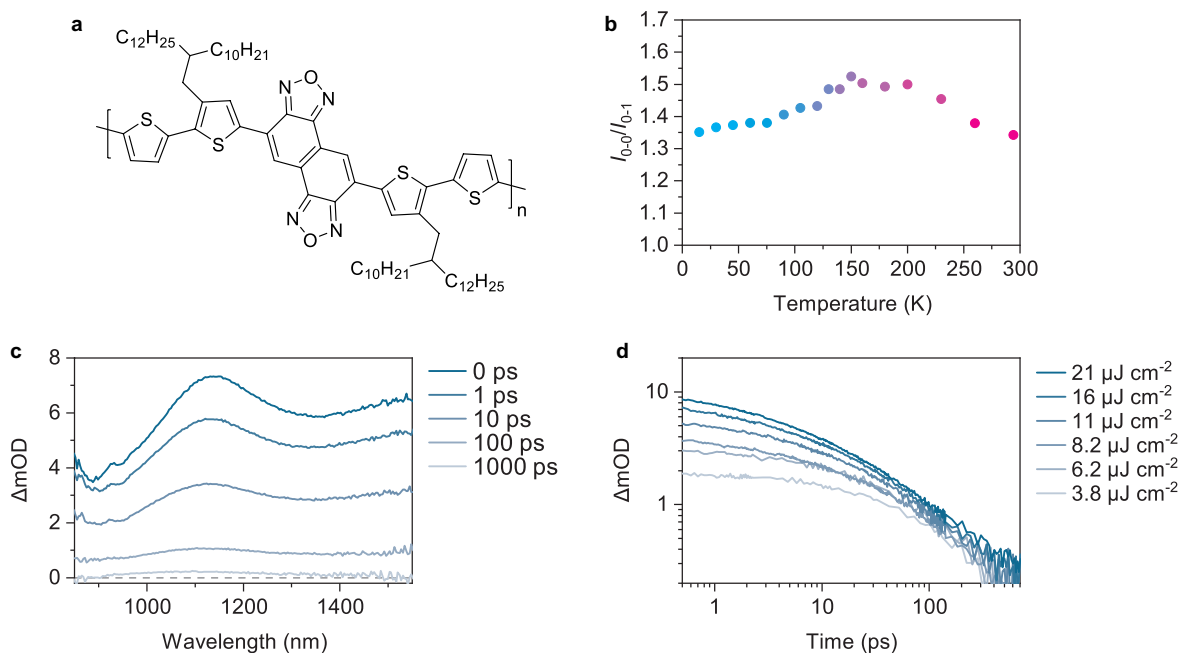
Figure 1. (a) Chemical structure of PNOz4T. (b) Temperature dependence of the PL intensity ratio I_{0-0}/I_{0-1}, where I_{0-0} and I_{1-1} represent the PL intensities of the 0–0 and 0–1 emission bands, respectively. (c) TA spectra of a pristine PNOz4T film. The excitation wavelength was set to 750 nm with a fluence of 11 μJ cm^{-2}. (d) Excitation fluence dependence of the exciton decay kinetics monitored at 1400 nm. Figures 1b–d are adapted with permission from ref. 14. Copyright 2020 American Chemical Society.

Photophysical properties of PNOz4T. Before presenting a detailed analysis of the 2D diffusion properties, a brief summary of previous reports on the photophysical properties of PNOz4T is discussed. The experimental data presented here were obtained from our previous report.[14] Figure 1b shows the temperature dependence of the photoluminescence (PL) intensity ratio I_{0-0}/I_{0-1} of a pristine PNOz4T film, where I_{0-0} and I_{1-1} represent the PL intensities of the 0–0 and 0–1 emission bands, respectively. The I_{0-0}/I_{0-1} value increases

with a decrease in temperature until 150 K, and then decreases with a decrease in temperature below 150 K. This complex temperature dependence is a characteristic of the HJ-aggregate proposed by Spano et al., who considered intrachain interaction as J-coupling, whereas interchain interaction was described as H-coupling.[22-27] In this model, the PL intensity ratio peaks at a threshold temperature as a coopetition between an H-like thermally activated term and a J-like thermally de-activated term. Therefore, we conclude that PNOz4T is likely to form HJ-aggregates owing to its relatively high backbone planarity. From the temperature dependence of the PL intensity ratio I_{0-0}/I_{0-1}, the intrachain exciton coupling J_{intra} is larger than the interchain coupling J_{inter} by a factor of ~2.8.[14]

Figure 1c shows the TA spectra of the pristine PNOz4T film, wherein the broad photoinduced absorption band in the near-IR region observed immediately after photoexcitation is attributable to singlet excitons. Singlet excitons decay faster with the increase in excitation fluence (Figure 1d), indicating the contribution of SSA. In contrast, exciton decay is independent of the excitation fluence at later times (approximately >150 ps),[14] indicating the absence of SSA. The intrinsic exciton lifetime τ at each temperature was determined by fitting the later time decay with an exponential function, as summarized in Table S1.

Simulated annealing (SA). The rate equation for singlet excitons including SSA is given as

$$\frac{\mathrm{d}n(t)}{\mathrm{d}t} = -kn(t) - \frac{1}{2}\gamma(t)n(t)^2 \tag{1}$$

where $n(t)$, k, and $\gamma(t)$ are the singlet exciton density at time t after photoexcitation, rate constant of monomolecular deactivation given by the inverse of τ, and rate coefficient of SSA, respectively. This equation is solved as

$$n(t) = \frac{n_0 \exp(-kt)}{1 + \frac{n_0}{2} \int_0^t \gamma(t)\exp(-kt)\mathrm{d}t}$$

(2)

where n_0 represents the exciton density at time 0. Because SSA is a diffusion-limited process, the rate coefficient $\gamma(t)$ is strongly dependent on the diffusion properties of excitons. As described in the Supporting Information in detail, there exists no simple analytical formula for $\gamma(t)$ for anisotropic 2D diffusion because of symmetry reduction, which is the origin of the difficulty of data analysis in our previous study.

In the absence of a simple analytical formula, numerical approaches are usually applied, wherein gradient decent algorithms are often used for optimization. However, it is well-known that this often fails to provide the global minimum solution when the objective function is complicated because it is easily trapped at the local minima (Figure S2). Therefore, we used a SA metaheuristic in this study to obtain the global minimum solution of the complicated exciton diffusion dynamics. SA metaheuristic is an analogy of the annealing of solids in condensed matter physics in which a solid is heated in a heat bath by increasing the temperature of the heat bath at which all particles of the solid can arrange themselves in the liquid phase, followed by cooling by slowly decreasing the temperature of the heat bath. Through this approach, all the particles arrange themselves in the most stable state. SA metaheuristic mimics these procedures to approximate the global optimization of an objective function, as shown schematically in Figure 2.[16,28-30] This method is based on the Metropolis–Hastings (MH) algorithm in the framework of the Markov chain Monte Carlo (MCMC) method for obtaining random ensembles from a (complicated) probability distribution.[31,32]

The algorithm proceeds as follows: First, we set an initial N-dimensional vector w and an objective function $f(w)$. In this study, $w = (D_x, D_y, R)$ and $f(w)$ is
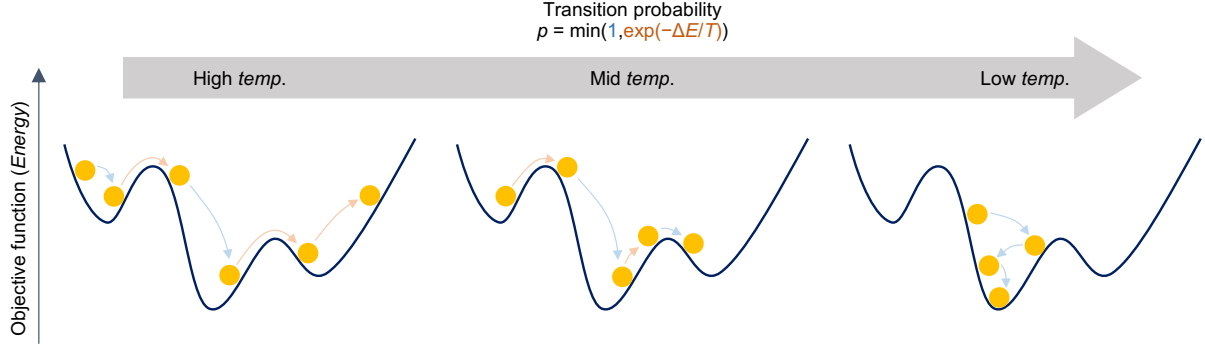
Figure 2. Schematic showing a simulated annealing (SA) metaheuristic. At each step, the SA metaheuristic proposes a new state θ from the vicinity of the current state w. When the objective function, i.e., *energy*, of the proposed state is lower than that of the current state, the proposed state will always be accepted to move (transition probability $p = 1$), as in the case of the conventional gradient descent algorithm. On the other hand, unlike in the gradient descent algorithm, the proposed state will be accepted with a probability of $\exp(-\Delta E/T)$ even when the *energy* of the proposed state is higher than that of the current state. This enables it to be de-trapped from the local minima if the *temperature* is sufficiently high. In contrast, the acceptance probability of uphill transition will be decreased with the decrease in *temperature*. Gradually lowering the *temperature* will eventually ensure that the uphill transition is almost rejected, and the SA metaheuristic behaves like the conventional gradient descent algorithm, at which time the initial state would already be in the vicinity of the destination, allowing it to reach the global minimum.

$$f(w) = \left(n_{obsd.} - n_{calcd.}(w)\right)^{\mathrm{T}} \cdot L \cdot \left(n_{obsd.} - n_{calcd.}(w)\right) \tag{3}$$

where X^{T} denotes the transpose matrix of X, D_x and D_y are the diffusion constants along the *x*- and *y*-axes, respectively, R is the effective reaction radius of singlet excitons, $n_{obsd.} \in \mathbb{R}^m$ is the experimentally observed exciton density, and $n_{calcd.} \in \mathbb{R}^m$ is the calculated exciton density using

Equation 2,[9,14,33] where $\gamma(t)$ obtained by the 2D diffusion model with an input parameter w is used (see the Supporting Information for more details). $L \in \mathbb{R}^{m \times m}$ is a diagonal matrix; each element of L is the inverse of the square of $n_{obsd.}$ to normalize widely varying values.

Then, the algorithm constructs a sample sequence of a Markov chain as follows (details can be found in the Supporting Information, Scheme S1):

I. Propose a new vector θ in the vicinity of w. Here, we used a random walk method to generate θ, where θ is given by

$$\vartheta = w + \delta \tag{4}$$

where the range of the steady distribution of δ can be different for each parameter.

II. Calculate the difference in the objective function. Here, we refer to the "*energy*" difference ΔE as an analogy of condensed matter physics, where the word "*energy*" is italicized to distinguish it from the energy in the real world. ΔE is expressed as

$$\Delta E = f(\vartheta) - f(w) \tag{5}$$

III. Perform the Metropolis test in which the proposed vector θ will be accepted as a new w for the next iteration with a probability of $\min(1, \exp(-\Delta E/T))$, where T is the "*temperature*" (italicized as well to distinguish it from the absolute temperature in the real world). In other words, the proposed vector θ will always be accepted when $\Delta E \leqq 0$, as in the case of the gradient descent algorithm. On the other hand, unlike in the gradient descent algorithm, the proposed vector will be accepted with a probability of $\exp(-\Delta E/T)$ even when $\Delta E > 0$, which enables it to be de-trapped from a local minimum if T is sufficiently high.

IV. Iterate (I)–(III) a certain number of times to obtain a probability density function (PDF) and find the temporal best solution, which is used as an initial vector for the next step.

V. Decrease the *temperature* according to a cooling schedule and restart the above algorithm with the initial vector obtained in step (IV).

VI. As the *temperature* decreases, so does the frequency of acceptance; therefore, we expect to reach a global minimum of $f(w)$ as the *temperature* approaches 0.

Applying this algorithm to the $n(t)$ curve gives an optimized solution of (D_x, D_y, R). Note that R was determined to be 3.5 nm for 294 K and 235 K (*vide infra*); thereby, R was fixed as this value at lower temperatures because exciton diffusion along the π-stacking direction is suppressed at lower temperatures (*vide infra*), resulting in quasi-1D diffusion, which is undesirable to determine D and R simultaneously because the rate equation then becomes an underdetermined system.

Two-dimensional singlet exciton diffusion. Figure 3 shows the time evolution of the exciton density $n(t)$ and annihilation rate coefficient $\gamma(t)$ calculated using the best solution of (D_x, D_y, R) obtained from the SA optimization. The obtained $\gamma(t)$ can well reproduce the experimentally obtained $n(t)$. It is worth noting that $\gamma(t)$ obtained in this study is almost identical to that obtained in our previous study using a genetic algorithm (GA)[34] (Figure S6). In our previous study, we performed a reverse analysis using a GA in which the algorithm explores the best solution of $\gamma(t)$ that successfully reproduces the experimental decay curve without any assumption about the diffusion properties. The good agreement between the two $\gamma(t)$ indicates that the SA approach with the 2D diffusion model successfully reproduced the diffusion behavior of singlet excitons in PNOz4T films. From the optimization, we obtained D_h of 9.8×10^{-3} cm^2 s^{-1}, D_l of 7.7×10^{-3} cm^2 s^{-1}, and R of 3.5 nm, where D_h (D_l) is the diffusion constant of the faster (slower) direction. It is worth noting that, since there exists no robust method for determining R, its value is usually assumed and hence can be a significant source of uncertainty.[35,36] In contrast, the effective
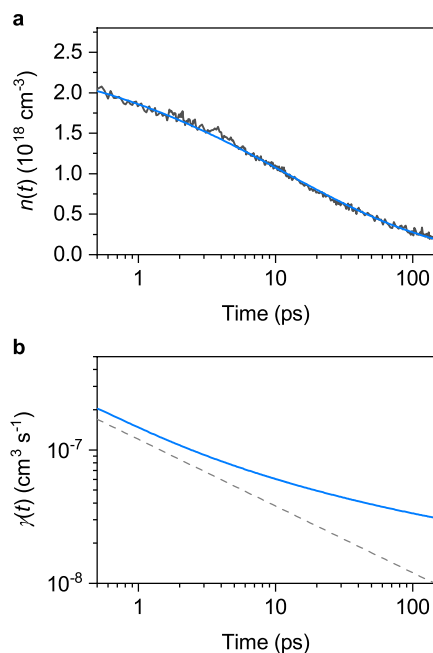
Figure 3. (a) Measured (black) and reproduced (blue) exciton decay kinetics. (b) Annihilation rate coefficient $\gamma(t)$ calculated using the optimized parameters w. The broken line represents the $t^{-1/2}$ dependence as a guide for the eye (see the Supporting Information).

reaction radius R is a fitting parameter in this algorithm, which means that the SA algorithm enables us to analyze the exciton decay kinetics without any assumptions for R (further discussion can be found in the Supporting Information). Another important advantage of this algorithm is its robustness: the algorithm always reaches the global minimum solution irrespective of the initial condition (see the Supporting Information for more details). Interestingly, the diffusion constants of the two directions are almost identical at room temperature (294 K), indicating that intrachain exciton motion can compete with that in the π-stacking direction in PNOz4T films, unlike the result in previous studies, as mentioned above.
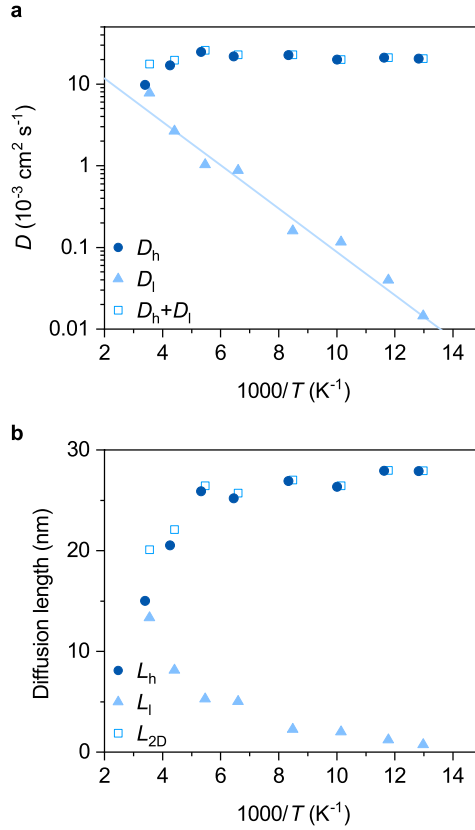
Figure 4. Temperature dependence of the (a) diffusion constant and (b) diffusion length. Closed triangles and open squares are slightly shifted horizontally to prevent overlap. L_h and L_l represent the diffusion length along the faster and slower directions, defined as $L_{h,l} = (D_{h,l}\tau)^{0.5}$. L_{2D} is the 2D diffusion length, defined as $L_{2D}^2 = L_h^2 + L_l^2$.

Temperature dependence of singlet exciton diffusion. Figure 4 shows the Arrhenius plot for the diffusion constants of the two directions extracted from the SA approach ($n(t)$ curve for each temperature can be found in the Supporting Information, Figure S7) and diffusion lengths obtained using D and τ. D_l decreased rapidly with the decrease in temperature. Such thermally activated diffusion characteristic is typical for conjugated polymers, as reported previously.[37] By applying Arrhenius fit with Equation 6, the activation energy E_a for D_l was determined to be ~53 meV.

$$D_l(T) \propto \exp\left(-\frac{E_a}{k_B T}\right) \qquad (6)$$

Interestingly, D_h increased with the decrease in temperature until $T > 188$ K and remained almost constant at lower temperatures. The peak D_h value is 24.9×10^{-3} cm^2 s^{-1} at 188 K, which is one order of magnitude larger than typical values for conjugated polymers[2] and similar to those of recent novel nonfullerene acceptors.[38-40] As a result, the diffusion length of excitons increases at low temperatures.

The question remained of the direction in which the diffusion is faster. An important finding from our previous study,[14] wherein we examined the temperature dependence of exciton decay generated in PNOz4T nanofibrils, is that the diffusion along the π-stacking direction is suppressed owing to spatial confinement (see the Supporting Information for more details). Interestingly, exciton decay kinetics in PNOz4T nanofibrils are less sensitive to temperature. Therefore, although there is currently no definitive experimental evidence, we presume that temperature-insensitive D_h represents the diffusion constant for the backbone direction and temperature-sensitive D_l for the π-stacking direction. We hope that an ongoing study will determine the direction. In the ongoing study, various conjugated polymer films with systematically controlled intra- and interchain exciton couplings were prepared, and the exciton dynamics were measured. Although we are still performing a detailed analysis, we have captured the systematic changes in diffusion dynamics depending on the exciton couplings. We will present these results as a separate paper because the main aim of the present study is to demonstrate the SA metaheuristic for exciton diffusion analysis.

Importantly, the temperature dependence for the faster direction cannot be rationalized by the Förster mechanism because the overlap integral between the absorption and PL spectra

decreases with a decrease in temperature (Figure S8). Instead, the efficient exciton motion at low temperatures is similar to the coherent transport of excitons. The coherent transport of singlet excitons in semiconducting polymers has been experimentally and theoretically investigated.[17-21] At low temperatures, the excitonic density of states becomes narrower because the disorder induced by molecular vibration decreases, resulting in an increase in the coherent component to exciton motion.

In summary, we demonstrated a detailed analysis of exciton diffusion properties using a SA metaheuristic with a 2D diffusion model. The anisotropic exciton diffusion properties were successfully revealed by the SA algorithm. We revealed that intrachain exciton diffusion can compete with that in the π-stacking direction in PNOz4T films with HJ-aggregate property. Exciton motion along the faster direction cannot be rationalized by a simple hopping picture. Based on the temperature dependence of the diffusion constant, we consider that coherent transport partly contributes to the exciton motion. As a result, the diffusion length is longer at low temperatures. To the best of our knowledge, this study is the first to provide clear evidence of thermally de-activated exciton diffusion in semi-crystalline conjugated polymer films.

ASSOCIATED CONTENT

Supporting Information.

The following files are available free of charge.

Analytical model, temperature dependence of intrinsic exciton lifetime, local minima issue for the gradient decent algorithm, workflow of SA algorithm, robustness of SA algorithm, effective

reaction radius, coincidence of the extracted $\gamma(t)$, temperature dependence, exciton diffusion in PNOz4T nanoaggregate, overlap integral (PDF)

AUTHOR INFORMATION

Notes

The authors declare no competing financial interests.

ACKNOWLEDGMENT

REFERENCES

1. Menke, S. M.; Holmes, R. J. Exciton Diffusion in Organic Photovoltaic Cells. *Energy Environ. Sci.* **2014,** *7*, 499-512.

2. Tamai, Y.; Ohkita, H.; Benten, H.; Ito, S. Exciton Diffusion in Conjugated Polymers: From Fundamental Understanding to Improvement in Photovoltaic Conversion Efficiency. *J. Phys. Chem. Lett.* **2015,** *6*, 3417-3428.

3. Mikhnenko, O. V.; Blom, P. W. M.; Nguyen, T.-Q. Exciton Diffusion in Organic Semiconductors. *Energy Environ. Sci.* **2015,** *8*, 1867-1888.

4. Hedley, G. J.; Ruseckas, A.; Samuel, I. D. Light Harvesting for Organic Photovoltaics. *Chem. Rev.* **2017,** *117*, 796-837.

5. Hennebicq, E.; Pourtois, G.; Scholes, G. D.; Herz, L. M.; Russell, D. M.; Silva, C.; Setayesh, S.; Grimsdale, A. C.; Müllen, K.; Brédas, J.-L.; Beljonne, D. Exciton Migration in Rigid-Rod Conjugated Polymers: An Improved Förster Model. *J. Am. Chem. Soc.* **2005,** *127*, 4744-4762.

6. Markov, D. E.; Blom, P. W. M. Anisotropy of Exciton Migration in Poly(*p*-phenylene vinylene). *Phys. Rev. B* **2006,** *74*, 085206.

7. Van Averbeke, B.; Beljonne, D.; Hennebicq, E. Energy Transport Along Conjugated Polymer Chains: Through-Space or through-Bond? *Adv. Funct. Mater.* **2008,** *18*, 492-498.

8. Shekhar, S.; Aharon, E.; Tian, N.; Galbrecht, F.; Scherf, U.; Holder, E.; Frey, G. L. Decoupling 2D Inter- and Intrachain Energy Transfer in Conjugated Polymers. *ChemPhysChem* **2009,** *10*, 576-581.

9. Tamai, Y.; Matsuura, Y.; Ohkita, H.; Benten, H.; Ito, S. One-Dimensional Singlet Exciton Diffusion in Poly(3-hexylthiophene) Crystalline Domains. *J. Phys. Chem. Lett.* **2014,** *5*, 399-403.

10. Bjorgaard, J. A.; Köse, M. E. Simulations of Exciton Diffusion and Trapping in Semicrystalline Morphologies of Poly(3-hexylthiophene). *J. Phys. Chem. C* **2014,** *118*, 5756-5761.

11. Ohkita, H.; Tamai, Y.; Benten, H.; Ito, S. Transient Absorption Spectroscopy for Polymer Solar Cells. *IEEE J. Sel. Top. Quantum Electron.* **2016,** *22*, 100-111.

12. Kawashima, K.; Osaka, I.; Takimiya, K. Effect of Chalcogen Atom on the Properties of Naphthobischalcogenadiazole-Based π-Conjugated Polymers. *Chem. Mater.* **2015,** *27*, 6558-6570.

13. Kawashima, K.; Tamai, Y.; Ohkita, H.; Osaka, I.; Takimiya, K. High-Efficiency Polymer Solar Cells with Small Photon Energy Loss. *Nat. Commun.* **2015,** *6*, 10085.

14. Murata, Y.; Takeyama, T.; Sakamoto, Y.; Yamaguchi, K.; Tamai, Y.; Ohkita, H. Two-Dimensional Exciton Diffusion in an HJ-Aggregate of Naphthobisoxadiazole-Based Copolymer Films. *J. Phys. Chem. C* **2020,** *124*, 13063-13070.

15. Sneyd, A. J.; Fukui, T.; Paleček, D.; Prodhan, S.; Wagner, I.; Zhang, Y.; Sung, J.; Collins, S. M.; Slater, T. J. A.; Andaji-Garmaroudi, Z.; MacFarlane, L. R.; Garcia-Hernandez, J. D.; Wang, L.; Whittell, G. R.; Hodgkiss, J. M.; Chen, K.; Beljonne, D.; Manners, I.; Friend, R. H.; Rao, A. Efficient Energy Transport in an Organic Semiconductor Mediated by Transient Exciton Delocalization. *Sci. Adv.* **2021,** *7*, eabh4232.

16. Kirkpatrick, S.; Gelatt, C. D.; Vecchi, M. P. Optimization by Simulated Annealing. *Science* **1983,** *220*, 671-680.

17. Collini, E.; Scholes, G. D. Coherent Intrachain Energy Migration in a Conjugated Polymer at Room Temperature. *Science* **2009,** *323*, 369-373.

18. Jin, X.-H.; Price, M. B.; Finnegan, J. R.; Boott, C. E.; Richter, J. M.; Rao, A.; Menke, S. M.; Friend, R. H.; Whittell, G. R.; Manners, I. Long-Range Exciton Transport in Conjugated Polymer Nanofibers Prepared by Seeded Growth. *Science* **2018,** *360*, 897-900.

19. Maiolo, F. D.; Brey, D.; Binder, R.; Burghardt, I. Quantum Dynamical Simulations of Intra-Chain Exciton Diffusion in an Oligo (para-phenylene vinylene) Chain at Finite Temperature. *J. Chem. Phys.* **2020,** *153*, 184107.

20. Pandya, R.; Alvertis, A. M.; Gu, Q.; Sung, J.; Legrand, L.; Kréher, D.; Barisien, T.; Chin, A. W.; Schnedermann, C.; Rao, A. Exciton Diffusion in Highly-Ordered One Dimensional Conjugated Polymers: Effects of Back-Bone Torsion, Electronic Symmetry, Phonons and Annihilation. *J. Phys. Chem. Lett.* **2021,** *12*, 3669-3678.

21. Prodhan, S.; Giannini, S.; Wang, L.; Beljonne, D. Long-Range Interactions Boost Singlet Exciton Diffusion in Nanofibers of π-Extended Polymer Chains. *J. Phys. Chem. Lett.* **2021,** *12*, 8188-8193.

22. Yamagata, H.; Spano, F. C. Interplay between Intrachain and Interchain Interactions in Semiconducting Polymer Assemblies: The HJ-Aggregate Model. *J. Chem. Phys.* **2012,** *136*, 184901.

23. Paquin, F.; Yamagata, H.; Hestand, N. J.; Sakowicz, M.; Bérubé, N.; Côté, M.; Reynolds, L. X.; Haque, S. A.; Stingelin, N.; Spano, F. C.; Silva, C. Two-Dimensional Spatial Coherence of Excitons in Semicrystalline Polymeric Semiconductors: Effect of Molecular Weight. *Phys. Rev. B* **2013,** *88*, 155202.

24. Müller, M.; Paulheim, A.; Eisfeld, A.; Sokolowski, M. Finite Size Line Broadening and Superradiance of Optical Transitions in Two Dimensional Long-Range Ordered Molecular Aggregates. *J. Chem. Phys.* **2013,** *139*, 044302.

25. Spano, F. C.; Silva, C. H- and J-Aggregate Behavior in Polymeric Semiconductors. *Annu. Rev. Phys. Chem.* **2014,** *65*, 477-500.

26. Eisfeld, A.; Marquardt, C.; Paulheim, A.; Sokolowski, M. Superradiance from Two Dimensional Brick-Wall Aggregates of Dye Molecules: The Role of Size and Shape for the Temperature Dependence. *Phys. Rev. Lett.* **2017,** *119*, 097402.

27. Wei, Y.-C.; Shen, S.-W.; Wu, C.-H.; Ho, S.-Y.; Zhang, Z.; Wu, C.-I.; Chou, P.-T. Through-Space Exciton Delocalization in Segregated HJ-Crystalline Molecular Aggregates. *J. Phys. Chem. A* **2021,** *125*, 943-953.

28. Ingber, L. Simulated Annealing: Practice Versus Theory. *Math. Comput. Model.* **1993,** *18*, 29-57.

29. Bertsimas, D.; Tsitsiklis, J. Simulated Annealing. *Stat. Sci.* **1993,** *8*, 10-15, 16.

30. Rutenbar, R. A. Simulated Annealing Algorithms: An Overview. *IEEE Circuits and Devices Magazine* **1989,** *5*, 19-26.

31. Chib, S.; Greenberg, E. Understanding the Metropolis-Hastings Algorithm. *Am. Stat.* **1995,** *49*, 327-335.

32. Geyer, C. J. Practical Markov Chain Monte Carlo. *Stat. Sci.* **1992,** *7*, 473-483.

33. Engel, E.; Leo, K.; Hoffmann, M. Ultrafast Relaxation and Exciton-Exciton Annihilation in PTCDA Thin Films at High Excitation Densities. *Chem. Phys.* **2006,** *325*, 170-177.

34. Whitley, D. A Genetic Algorithm Tutorial. *Stat. and Comput.* **1994,** *4*, 65-85.

35. Cook, S.; Liyuan, H.; Furube, A.; Katoh, R. Singlet Annihilation in Films of Regioregular Poly(3-hexylthiophene): Estimates for Singlet Diffusion Lengths and the Correlation between Singlet Annihilation Rates and Spectral Relaxation. *J. Phys. Chem. C* **2010,** *114*, 10962-10968.

36. Chowdhury, M.; Sajjad, M. T.; Savikhin, V.; Hergué, N.; Sutija, K. B.; Oosterhout, S. D.; Toney, M. F.; Dubois, P.; Ruseckas, A.; Samuel, I. D. W. Tuning Crystalline Ordering by Annealing and Additives to Study Its Effect on Exciton Diffusion in a Polyalkylthiophene Copolymer. *Phys. Chem. Chem. Phys.* **2017,** *19*, 12441-12451.

37. Mikhnenko, O. V.; Cordella, F.; Sieval, A. B.; Hummelen, J. C.; Blom, P. W. M.; Loi, M. A. Temperature Dependence of Exciton Diffusion in Conjugated Polymers. *J. Phys. Chem. B* **2008,** *112*, 11601-11604.

38. Chandrabose, S.; Chen, K.; Barker, A. J.; Sutton, J. J.; Prasad, S. K. K.; Zhu, J.; Zhou, J.; Gordon, K. C.; Xie, Z.; Zhan, X.; Hodgkiss, J. M. High Exciton Diffusion Coefficients in Fused Ring Electron Acceptor Films. *J. Am. Chem. Soc.* **2019,** *141*, 6922-6929.

39. Firdaus, Y.; Le Corre, V. M.; Karuthedath, S.; Liu, W.; Markina, A.; Huang, W.; Chattopadhyay, S.; Nahid, M. M.; Nugraha, M. I.; Lin, Y.; Seitkhan, A.; Basu, A.; Zhang, W.; McCulloch, I.; Ade, H.; Labram, J.; Laquai, F.; Andrienko, D.; Koster, L. J. A.; Anthopoulos, T. D. Long-Range Exciton Diffusion in Molecular Non-Fullerene Acceptors. *Nat. Commun.* **2020,** *11*, 5220.

40. Natsuda, S.; Sakamoto, Y.; Takeyama, T.; Shirouchi, R.; Saito, T.; Tamai, Y.; Ohkita, H. Singlet and Triplet Excited-State Dynamics of a Nonfullerene Electron Acceptor Y6. *J. Phys. Chem. C* **2021**, *125*, 20806-20813.

Supporting Information for

Intrachain Exciton Motion Can Compete with Interchain Hopping in Conjugated Polymer Films with a Strong J-aggregate Property

Yasuhiro Murata[1] and Yasunari Tamai[1,2*]

[1] Department of Polymer Chemistry, Graduate School of Engineering, Kyoto University, Katsura, Nishikyo, Kyoto 615-8510, Japan

[2] Japan Science and Technology Agency (JST), PRESTO, 4-1-8 Honcho Kawaguchi, Saitama 332-0012, Japan

*Corresponding author: tamai@photo.polym.kyoto-u.ac.jp

Analytical model

The rate equation for singlet excitons including SSA is given as

$$\frac{\mathrm{d}n(t)}{\mathrm{d}t} = -kn(t) - \frac{1}{2}\gamma(t)n(t)^2 \tag{S1}$$

where $n(t)$, k, and $\gamma(t)$ are the singlet exciton density at time t after photoexcitation, rate constant of monomolecular deactivation given by the inverse of the exciton lifetime τ, and rate coefficient of SSA, respectively. This equation is solved as

$$n(t) = \frac{n_0\exp(-kt)}{1 + \frac{n_0}{2}\int_0^t \gamma(t)\exp(-kt)\mathrm{d}t} \tag{S2}$$

where n_0 represents the exciton density at time 0.

Because SSA is a diffusion-limited process, the rate coefficient $\gamma(t)$ is strongly dependent on the diffusion properties of excitons. $\gamma(t)$ is a function of the dimensionality of exciton diffusion, as summarized in our previous study.[S1,S2] For instance, $\gamma(t)$ in three-dimensional (3D) and one-dimensional (1D) systems are given as

$$\gamma_{3D}(t) = 8\pi DR\left(1 + \frac{R}{\sqrt{2\pi Dt}}\right) \tag{S3}$$

$$\gamma_{1D}(t) = 4\pi DR\frac{R}{\sqrt{2\pi Dt}} \tag{S4}$$

where D is the diffusion constant and R is the effective reaction radius. This means that $\gamma(t)$ approaches a time-independent formula, $\gamma_{3D} = 8\pi DR$, when $t \gg R^2/(2\pi D)$ for the 3D system whereas it exhibits $t^{-1/2}$ dependence over the entire time domain in the 1D system. By substituting Equations S3 and S4 into S2, we obtain a simple analytical formula for $n(t)$; hence, we can successfully evaluate the diffusion properties using Equations S2–S4 for 3D and 1D diffusion systems.

In contrast, the situation is more complicated for the 2D system because of symmetry reduction.[S3] $\gamma(t)$ for the isotropic 2D system is given as

$$\gamma_{\mathrm{iso2D}}(t) = \frac{8DR}{\pi}\int_0^\infty \exp(-Du^2t)\frac{du}{u[J_0^2(uR) + Y_0^2(uR)]} \tag{S5}$$

where J_0 and Y_0 are the zero-order Bessel functions of the first and second kind, respectively. The situation is more complicated if we consider anisotropic 2D diffusion, wherein the diffusion constants along the two directions are different. Therefore, in this study, we used a numerical 2D diffusion model given below, instead of an analytical formula.

The associated diffusion equation is given as

$$\frac{\partial n(x,y,t)}{\partial t} = D_x \frac{\partial^2 n(x,y,t)}{\partial x^2} + D_y \frac{\partial^2 n(x,y,t)}{\partial y^2} \qquad (S6)$$

where $n(x,y,t)$ is the exciton density at location (x,y) and time t. D_x and D_y represent the diffusion constants along the x- and y-axes, respectively. In this study, we used an explicit method to solve the above equation. Applying finite difference approximation yields

$$\frac{u_{i,j}^{k+1} - u_{i,j}^{k}}{\Delta t} = D_x \frac{u_{i+1,j}^{k} - 2u_{i,j}^{k} + u_{i-1,j}^{k}}{(\Delta a)^2} + D_y \frac{u_{i,j+1}^{k} - 2u_{i,j}^{k} + u_{i,j-1}^{k}}{(\Delta a)^2} \qquad (S7)$$

where $u_{i,j}{}^{k}$ is the discrete function representing the exciton density at the i,j-th lattice at time step k. Thus, $u_{i,j}{}^{k+1}$ can be expressed as

$$u_{i,j}^{k+1} = u_{i,j}^{k} + \frac{D_x \Delta t}{(\Delta a)^2} (\cdots) + \frac{D_y \Delta t}{(\Delta a)^2} (u_{i,j+1}^{k} - 2u_{i,j}^{k} + u_{i,j-1}^{k}) \qquad (S8)$$

Equation S8 was numerically solv... D_y,R). A 2D grid with a length of 50 nm and Δa of 0.5 nm was used. Δt was se... the stability condition. The exciton density was always 0 inside the lattice... irichlet boundary condition), whereas the Neumann boundary condition (dn... daries (Figure S1).

$\gamma(t)$ is associated with the flux of... oss-section S as

$$\gamma_{2D}(t) = -\frac{S}{n_0}(J_x + J_y) = \frac{8R^2}{n_0}\left[D_x \frac{\partial n(x,y,t)}{\partial x} + D_y \frac{\partial n(x,y,t)}{\partial y} \right] \quad s.t. \ x = y = R \qquad (S9).$$
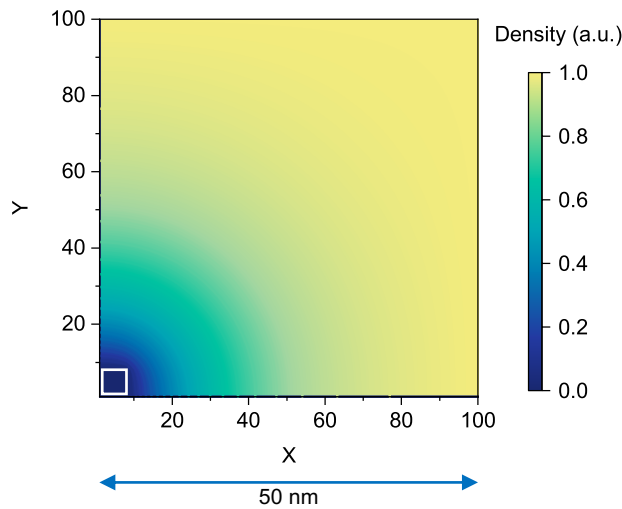

Figure S1. Schematic showing the 2D grid wherein excitons move in the X and Y directions. The exciton density is always 0 inside the white square with a length of R, whereas the Neumann boundary condition (dn/dt = 0) is used for other boundaries.

Temperature dependence of intrinsic exciton lifetime

The exciton lifetime τ in the absence of SSA at each temperature was determined by excitation fluence independent decay at later times by fitting with an exponential function, as summarized in Table S1.

Table S1. Intrinsic exciton lifetime at each temperature.

Temperature (K)	Lifetime (ps)
294	230
235	250
188	270
155	290
120	320
100	350
86	370
78	380

Local minima issue for the gradient decent algorithm

Figure S2 shows the histograms of the optimized parameters obtained using a gradient descent algorithm with random initial conditions. As mentioned in the main text, this algorithm fails to provide a robust solution.
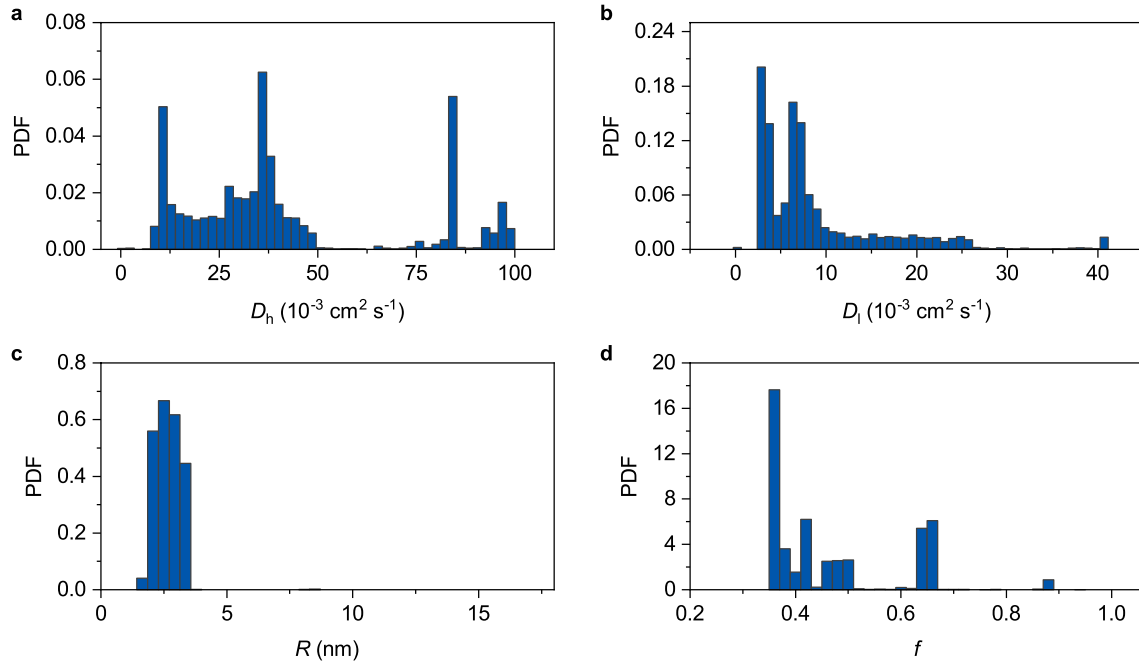

Figure S2. Histogram of (a) D_h, (b) D_l, (c) R, and (d) objective function f. The initial parameters of D_h, D_l, and R were randomly selected in the range of 0–50×10^{-3} cm^2 s^{-1}, 0–50×10^{-3} cm^2 s^{-1}, and 0–10 nm for D_h, D_l, and R, respectively. We calculated 10^4 data sets to obtain these histograms.

Workflow of SA algorithm

Scheme S1 represents the workflow of the SA algorithm used in this study. At each step, the SA metaheuristic proposes a new state θ from the vicinity of the current state w. When the *energy* of the proposed state is lower than that of the current state, the proposed state will always be accepted. On the other hand, the proposed state will be accepted with a probability of $\exp(-\Delta E/T)$ even when the *energy* of the proposed state is higher than that of the current state. Note that the proposed state will always be rejected when it contains negative values as it is physically meaningless. Gradually lowering the *temperature* will eventually ensure that the uphill transition is almost rejected, and the SA metaheuristic behaves like the conventional gradient descent algorithm, at which time the initial state would already be the vicinity of the destination, allowing it to reach the global minimum. Here, N threads of the computation run in parallel. In each thread, a Markov chain with a length of $K \times n$ was generated. Therefore, $100 \times 3 \times 32 \sim 10^4$ ensembles were generated at each *temperature*. The initial *temperature* was set so that the acceptance ratio (AR) of the Metropolis test of the first iteration was >0.8. The stopping criterion was set so that AR is <0.01 (see Figure S3 for more details). The exponential multiplicative monotonic cooling was adopted as $T_{new} = 0.8 \times T$. In the random-walk Metropolis–Hastings (RWMH) algorithm, δ_j^k is randomly selected from the stationary distribution $[-\delta_j, \delta_j]$, and the range of the steady distribution could be different for each parameter.
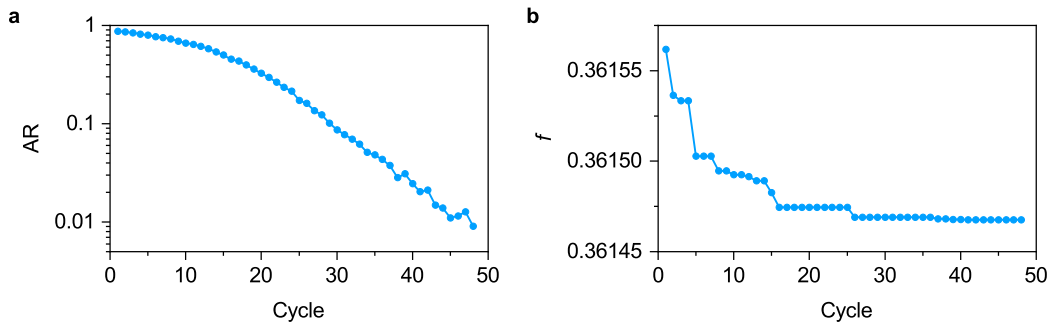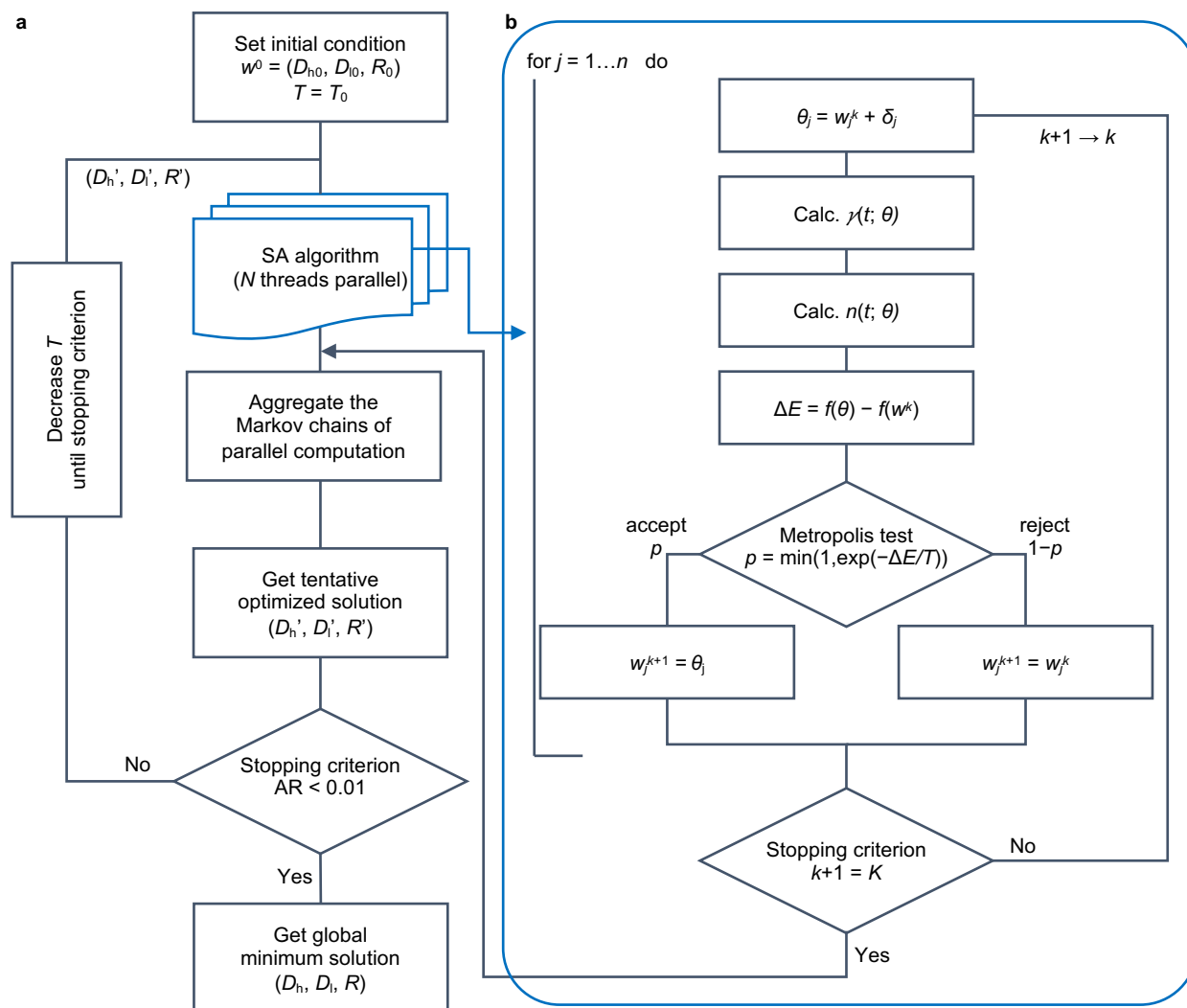

Figure S3. (a) Acceptance ratio of the Metropolis test (AR) and (b) objective function f for each cycle. The initial *temperature* (T at Cycle 1) is set so that AR of the first iteration is >0.8. When AR is less than 0.05, f hardly changes; thereby the stopping criterion is set so that AR is <0.01.

a

Set initial condition
$w^0 = (D_{h0}, D_{l0}, R_0)$
$T = T_0$

(D_h', D_l', R')

SA algorithm
(N threads parallel)

Decrease T until stopping criterion

Aggregate the Markov chains of parallel computation

Get tentative optimized solution
(D_h', D_l', R')

No — Stopping criterion
$AR < 0.01$

Yes

Get global minimum solution
(D_h, D_l, R)

b

for $j = 1…n$ do

$\theta_j = w_j^k + \delta_j$

$k+1 \rightarrow k$

Calc. $\gamma(t; \theta)$

Calc. $n(t; \theta)$

$\Delta E = f(\theta) - f(w^k)$

accept p — Metropolis test
$p = \min(1, \exp(-\Delta E/T))$ — reject $1-p$

$w_j^{k+1} = \theta_j$

$w_j^{k+1} = w_j^k$

Stopping criterion
$k+1 = K$ — No

Yes

Scheme S1. Schematic showing the (a) overall and (b) RWMH workflows of the SA algorithm. Here, $N = 32$, $n = 3$ (or 2 for low temperatures because R is fixed), and $K = 100$.
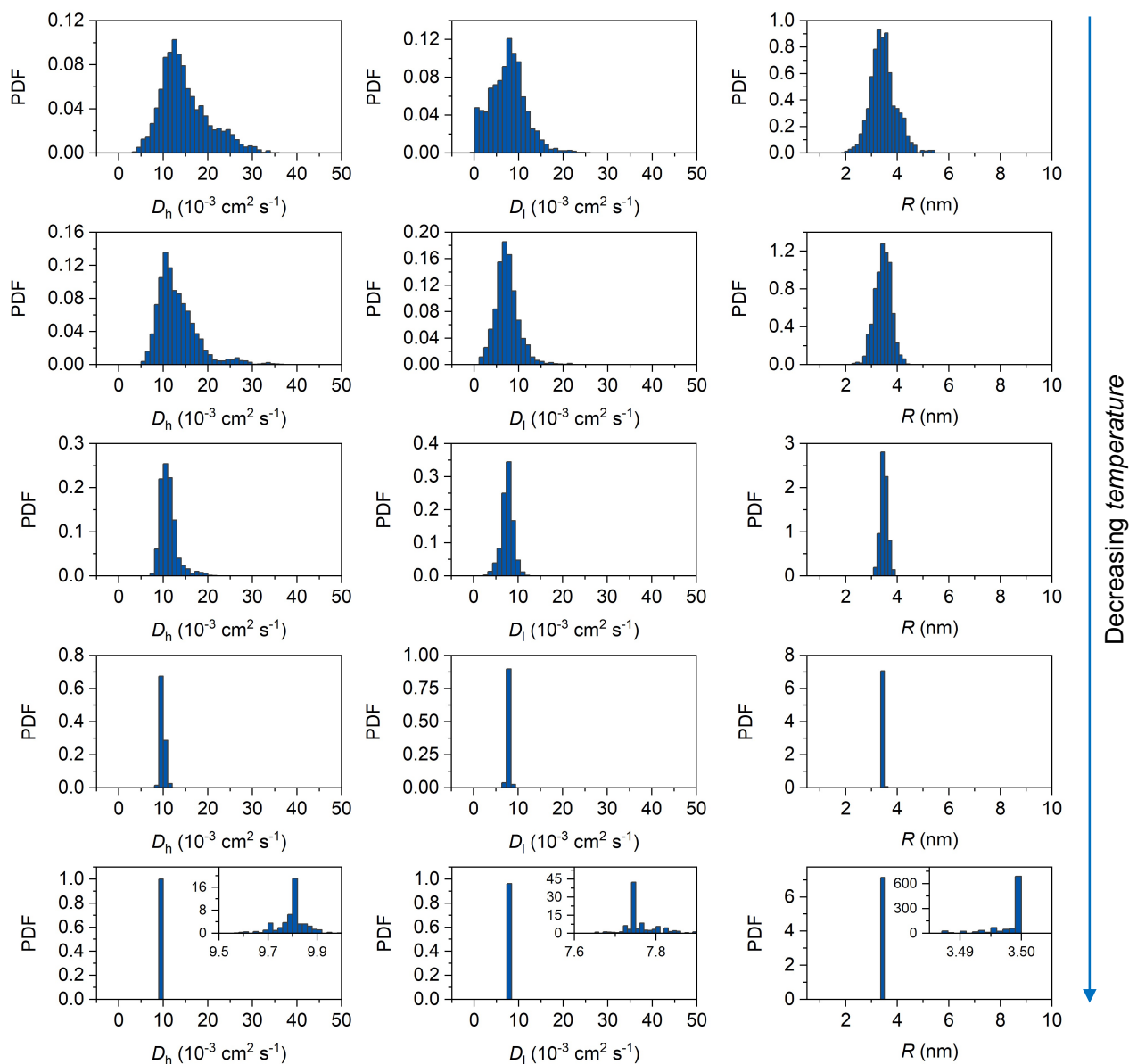
Figure S4. Histograms of D_h, D_l, and R in the Markov chain at each *temperature*. The insets in the bottom row are the enlarged view.

Robustness of SA algorithm

We examined the robustness of the SA algorithm by performing two sets of validations. We used MATLAB R2021a with double precision to run the algorithm. First, we performed a SA analysis with a plausible initial condition and an extensively large iteration number of $K = 1000$ (condition 1, Table S2). Then, we examined the same analysis with two different initial conditions to demonstrate that the SA algorithm can always reach the global minimum irrespective of the initial condition. We selected two extremely ill initial conditions (conditions 2 and 3). The SA algorithm always converges to the same solution, even when we started from the ill conditions (Table S3). Next, we repeated the same calculation (conditions 4–8) with the same initial conditions of "condition 1" but with a smaller iteration number K. The SA algorithm again converges to almost the same solution. If we assume that the value obtained by "condition 1" as the true value, the maximum relative errors in the conditions 4–8 are 0.13, 0.16, 1.8×10^{-3}, and 5.5×10^{-5}%, respectively, meaning that $K = 100$ is sufficient to obtain the robust solution when we start from a plausible initial condition. Therefore, we set $K = 100$ for lower temperatures to reduce the computational effort.

Table S2. Initial conditions.

Condition	D_{h0} (10^{-3} cm^2 s^{-1})	D_{l0} (10^{-3} cm^2 s^{-1})	R_0 (nm)	Number of iteration K
1	10	10	3.5	1000
2	0.1	0.1	0.1	1000
3	100	100	10	1000
4	10	10	3.5	100
5	10	10	3.5	100
6	10	10	3.5	100
7	10	10	3.5	100
8	10	10	3.5	100

Table S3. Robustness of SA algorithm.

Condition	D_h (10^{-3} cm^2 s^{-1})	D_l (10^{-3} cm^2 s^{-1})	R (nm)	f
1	9.82067047189678	7.72888859152443	3.49999412753973	0.361467637567055
2	9.81808797386164	7.73124539243516	3.49999853617459	0.361467628167083
3	9.81455067695460	7.73427895719002	3.49999456569898	0.361467650496503
4	9.81271216937498	7.73595710324777	3.49998926054091	0.361467672370337
5	9.82062882565569	7.72868914674232	3.49999887695914	0.361467631872672
6	9.81499904100226	7.73489930589031	3.49996494014844	0.361467754168745
7	9.82130219088652	7.72879307296208	3.49998987497244	0.361467653082073
8	9.80752872062849	7.74107934606171	3.49992942746849	0.361467837521605

Effective reaction radius

A major problem of the annihilation method for evaluating the diffusion constant is determining the effective reaction radius R. As mentioned in the main text, because there exists no robust method for determining R, its value is usually assumed, which can be a significant source of uncertainty. We previously proposed that R can be estimated based on the excitation fluence dependence of the initial TA signals.[1] We reported that R is 3.4 nm for P3HT. Direct observation of exciton diffusion using TAM has shown that this value is somewhat reasonable,[S4] but can still be a source of uncertainty. Here, we compared the experimentally estimated R with that from the SA algorithm. Figure S5 shows the initial exciton density plotted against the excitation fluence I_{ex}. The initial density increased linearly with the increase in I_{ex} at low excitation fluences (red line). In contrast, the slope is as low as 1/2 at high excitation fluences (blue line). This behavior is attributable to SSA "without" exciton diffusion because excitons are overcrowded in the film. From the intersection of the two lines, the threshold exciton density was determined to be 6.2×10^{18} cm^{-3}. R was estimated to be 3.4 nm by assuming excitons to be a sphere with a radius R. This value shows reasonable agreement with that obtained using the SA algorithm. (3.5 nm) This suggests that this method can be used as a rough estimation of R, but can still be a source of uncertainty.
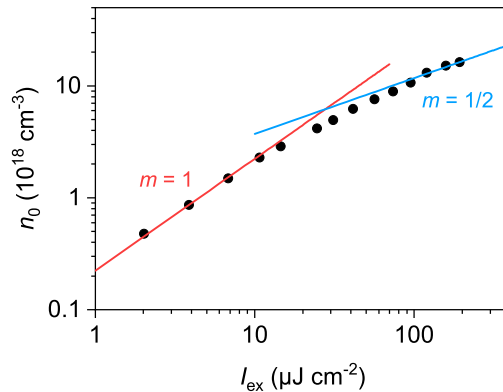

Figure S5. Log–log plots of the initial exciton density against the excitation fluence I_{ex}. The solid lines represent fitting curves with a power-law equation $\Delta OD \propto I_{ex}{}^{m}$.

Coincidence of the extracted $\gamma(t)$

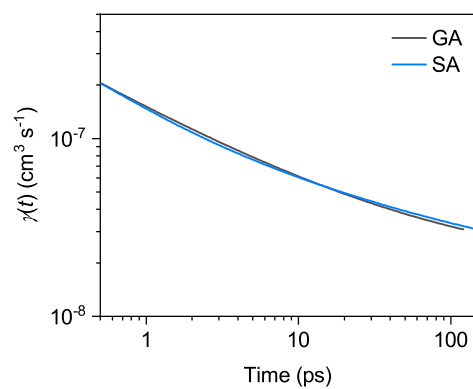**Figure S6**. Annihilation rate coefficients obtained in this study (blue) and our previous study (black)[S3].
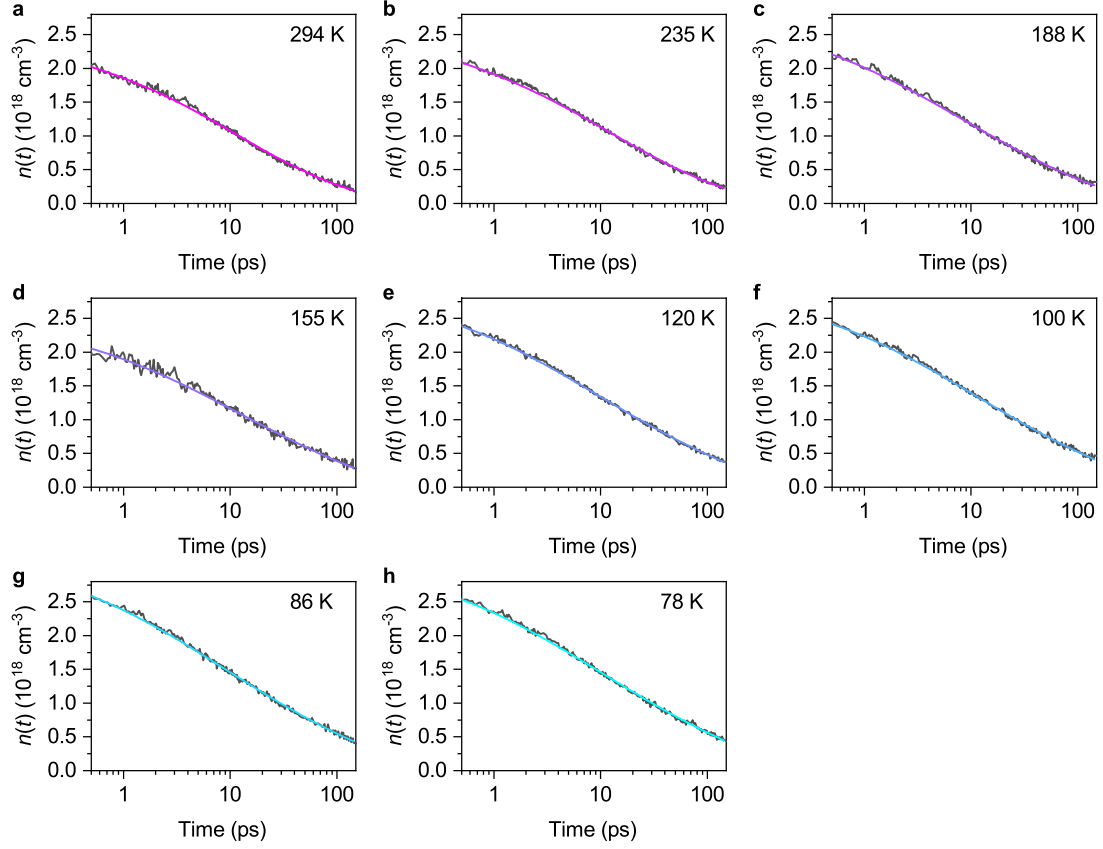
Temperature dependence

Figure S7. Measured (black) and reproduced (colored) exciton decay kinetics at various temperatures.

Table S4. Temperature dependence of each parameter.

Temp. (K)	D_h (10^{-3} cm² s⁻¹)	D_l (10^{-3} cm² s⁻¹)	$D_h + D_l$ (10^{-3} cm² s⁻¹)	L_h (nm)	L_l (nm)	L_{2D} (nm)
294	9.8	7.7	17.5	15.0	13.3	20.1
235	16.9	2.7	19.5	20.6	8.1	22.1
188	24.9	1.0	25.9	25.9	5.3	26.4
155	21.9	0.9	22.8	25.2	5.0	25.7
120	22.6	0.2	22.8	26.9	2.3	27.0
100	19.9	0.1	20.0	26.4	2.0	26.4
86	21.1	$(0.04)^a$	21.1	27.9	$(1.2)^a$	28.0
78	20.5	$(0.01)^a$	20.5	27.9	$(0.7)^a$	27.9

[a]: The values in parentheses are too small to be reliable.

Exciton diffusion in PNOz4T nanoaggregate

In our previous study, we performed TA measurements for PNOz4T in a chlorobenzene (CB) solution.[S3] PNOz4T does not fully dissolve in the CB solution because of poor solubility, but forms nanoaggregates in the CB solution, as reported previously.[S5] Singlet excitons in the CB solution decayed faster with the increase in excitation fluence, which is an indication of SSA in nanoaggregates.

The time dependence of $\gamma(t)$ in the CB solution was clearly different from that of the film state even though there was no large difference in the absorption and PL spectra between them: $\gamma(t)$ of the CB solution follows the $t^{-1/2}$ dependence, suggesting 1D exciton diffusion. This result indicates that excitons in the nanoaggregates can diffuse in only one of the two directions. Because the PL spectra of the CB solution is consistent with that of the film state, the backbone planarity and effective conjugation length of PNOz4T in the nanoaggregates are supposed to be comparable to those of the film state. In other words, excitons would be able to diffuse along the backbone direction in the CB solution as in the case of the film state. Therefore, we consider that excitons in the nanoaggregates diffuse predominantly along the backbone direction and cannot diffuse along the π-stacking direction because of lack of a long-range order in the π-stacking direction.

Strikingly, negligible temperature dependence was observed for the exciton decay kinetics in PNOz4T nanoaggregates. This temperature dependence cannot be rationalized by the activation energy of 53 meV obtained in this study for the slower diffusion constant D_l. Therefore, we presume that temperature insensitive diffusion (i.e., D_h) can be attributable to the exciton diffusion along the backbone direction.

Overlap integral

Figure S8 shows the temperature dependence of the absorption and PL spectra. As clearly shown in the figure, the overlap between these spectra was decreased with the decrease in temperature. We calculated the overlap integral J as follows to ensure a more quantitative comparison:

$$J = \int PL(\lambda)\, Abs.(\lambda)\lambda^4 \mathrm{d}\lambda \tag{S10}$$

where $Abs.(\lambda)$ is the absorption coefficient and $PL(\lambda)$ is the area normalized PL intensity. We found that J at 294 K is approximately 1.6 times larger than that at 78 K.
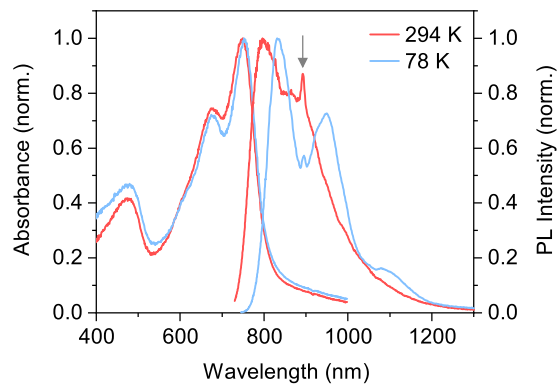

Figure S8. Temperature dependence of absorption and PL spectra. The sharp spike signal indicated by the arrow is an artifact from the equipment.

References

S1. Tamai, Y.; Matsuura, Y.; Ohkita, H.; Benten, H.; Ito, S. One-Dimensional Singlet Exciton Diffusion in Poly(3-hexylthiophene) Crystalline Domains. *J. Phys. Chem. Lett.* **2014,** *5*, 399-403.

S2. Tamai, Y.; Ohkita, H.; Benten, H.; Ito, S. Exciton Diffusion in Conjugated Polymers: From Fundamental Understanding to Improvement in Photovoltaic Conversion Efficiency. *J. Phys. Chem. Lett.* **2015,** *6*, 3417-3428.

S3. Murata, Y.; Takeyama, T.; Sakamoto, Y.; Yamaguchi, K.; Tamai, Y.; Ohkita, H. Two-Dimensional Exciton Diffusion in an HJ-Aggregate of Naphthobisoxadiazole-Based Copolymer Films. *J. Phys. Chem. C* **2020,** *124*, 13063-13070.

S4. Sneyd, A. J.; Fukui, T.; Paleček, D.; Prodhan, S.; Wagner, I.; Zhang, Y.; Sung, J.; Collins, S. M.; Slater, T. J. A.; Andaji-Garmaroudi, Z.; MacFarlane, L. R.; Garcia-Hernandez, J. D.; Wang, L.; Whittell, G. R.; Hodgkiss, J. M.; Chen, K.; Beljonne, D.; Manners, I.; Friend, R. H.; Rao, A. Efficient Energy Transport in an Organic Semiconductor Mediated by Transient Exciton Delocalization. *Sci. Adv.* **2021,** *7*, eabh4232.

S5. Kawashima, K.; Osaka, I.; Takimiya, K. Effect of Chalcogen Atom on the Properties of Naphthobischalcogenadiazole-Based π-Conjugated Polymers. *Chem. Mater.* **2015,** *27*, 6558-6570.